

A Laboratory Method for Measuring the Cross-Polarization in High-Contrast Imaging

Richard A. Frazin[†]

[†]Dept. of Climate and Space Sciences, University of Michigan, Ann Arbor, MI 48109

Abstract. Electric Field Conjugation (EFC) and related techniques have proven to be effective for high-contrast coronagraphic imaging, and they have applications in current and future exoplanet direct imaging missions. EFC utilizes one or more deformable mirrors (DMs) to nullify the electric fields from the host star within a designated “dark hole” region in the image plane, allowing for the detection of much fainter planetary emissions. The quality of a dark hole is quantified by the *contrast*, i.e., the planet-to-star intensity ratio, that could be measured inside it. Inside the dark hole, the planet’s light is distinguished from the residual starlight due to its *incoherence*; specifically, unlike starlight, the planetary light is essentially unmodulated by DM perturbations. *Cross polarization* can cause the modulation of the starlight to behave differently than predicted, and can limit the achievable contrast ratio, especially if it is not taken into account. The cause of cross polarization is the various weakly polarizing interactions of the light as it propagates through the optical system, notably reflections and finite focal length effects. Sophisticated physical optics software can model the cross polarization for a for a fully specified optical system, but this capability does not obviate the need for end-to-end measurements of the cross polarization.

This article presents realistic numerical simulations of a novel laboratory-based method for measurements of the cross-polarization in a coronagraphic optical system. This capability may well prove useful for validating models of polarization effects in future high-contrast imaging systems. The proposed laboratory method is not much more demanding than current efforts on the high-contrast testbeds, yet the simulation results demonstrate highly accurate estimates of the real and imaginary parts of the electric field corresponding to the cross polarization in a dark hole. These encouraging results suggest that laboratory implementation should be viable.

The proposed method uses a 100 mW supercontinuum laser with a narrow bandpass and two linear polarizers to isolate the cross polarization effects. A novel nonlinear probing scheme, along with nonlinear regression, is introduced to address polarizer leakage. Simulations are performed for an aberrated Lyot coronagraph with an f-number of 44, at a wavelength $\lambda = 1 \mu\text{m}$, using a single 33×33 actuator deformable mirror. The initial dark hole contrast is $\sim 10^{-10}$, with cross-polarization electric fields corresponding to intensities of $\sim 10^{-11}$ in contrast units. These cross-polarization electric fields are estimated simultaneously across 441 pixels, covering a patch approximately $4\lambda/D \times 4\lambda/D$ in the image plane.

The primary application of this method is likely laboratory validation of digital twin models for cross-polarization. On-sky, the experimentally validated models could then be used to account for cross polarization when estimating the planetary signal. Although speculative, an exciting future prospect is experimental validation of AI-based models that leverage conventional EFC sensing data to predict cross-polarization electric fields.

Keywords: stellar coronagraph, polarization, laboratory methods, numerical methods.

[†]Richard Frazin, rfrazin@umich.edu

1 Introduction

Direct imaging of exoplanets is among NASA’s top priorities in future missions, such as the Large UV/Optical/Infrared Surveyor (LUVOIR). The principal challenge of direct imaging is the fact that exoplanets are located in close angular proximity to their vastly brighter host stars. Quantitatively, this means that the telescopic optical system must be able to achieve a contrast ratio, i.e., planet-to-star brightness ratio, of less than 10^{-8} , or perhaps even 10^{-11} , depending on the target.¹ Current designs to meet this daunting requirement feature stellar coronagraphs, which extinguish on-axis light but allow slightly off-axis beams to pass through relatively unimpeded.² Even if the stellar coronagraphs had perfect optical surfaces, diffraction alone would put the contrast levels orders

of magnitude above the aforementioned requirements. Real surfaces have aberrations at high and low spatial frequencies that further degrade the contrast.³ Achieving high contrast requires active wavefront control strategies, also known as *adaptive optics*. In the space-based context, the most prominent of these is a family of methods that fall under the term *electric field conjugation (EFC)*. EFC procedures use one or two deformable mirrors (DMs) to modulate the intensity measured in the image plane through alternating sensing and control steps. The end result of EFC procedures is a region of the image plane called a *dark hole* in which the starlight is suppressed to a high contrast level.^{4,5} In test bed settings, such procedures yield dark holes with roughly 10^{-9} of the brightness of the laser source, which plays the role of a star.^{6,7}

EFC procedures are based on the fact that the starlight present at some level throughout the image plane is coherent, which allows the DM to modulate the intensity and create the dark hole, which is a region of destructive interference. Any exoplanet light present will be slightly off-axis and incoherent with the starlight. This incoherence is the key to detection of faint exoplanets, since the center of the exoplanet's image will not be modulated significantly by the DM.⁸ Thus, the portion of the light that is not modulated is ascribed to planetary emission. One limitation to the contrast that can be achieved via such procedures is imposed by polarization effects, which can be confounded with incoherence at very high contrast levels, as this article explains in detail later. Baudoz *et al.* argued that polarization aberration had an effect of $\sim 10^{-8}$ on the TDH2 bench.⁹ Further, polarization-dependent aberrations were part of a comprehensive study on the effect of aberrations the Roman Space Telescope Coronagraph, showing that 10^{-9} or better contrast is within reach by Krist *et al.*³

This article presents a concept for a relatively simple laboratory experiment and DM-based sensing algorithms that will allow DM modulation-based measurements of the electric fields corresponding to the polarization effects. The most likely use of these laboratory measurements is the validation of models of the cross-polarization, which is timely given the increasing importance of digital twin concepts in high-contrast imaging.¹⁰ At the simplest level, the proposed measurements could validate basic descriptive statistics (e.g., mean and variance) of the cross-polarization. More sophisticated would be validating AI-based models that map measurements of the fields made in course of classical EFC procedures to the cross-polarized electric fields.

1.1 Examples of Cross-Polarization in Simple Focusing Systems

It is generally appreciated that reflections can have polarization effects, which are calculated in a straightforward manner with the Fresnel coefficients for a plane wave reflecting from a planar surface.¹¹ Less well recognized is that the finite $f/\#$ (“f-number”) of a focusing optical system can convert some amount of one linear polarization into orthogonal linear polarization. We will refer to the generation of the orthogonal polarization via nominally unpolarized powered or planar optics as *cross-polarization*. To understand cross-polarization with powered optics, consider a collimated beam with diameter D propagating along the $+z$ axis and polarized in the x direction with field strength \sqrt{I} , where I is the intensity of the collimated beam. The light is then refracted by a thin lens with focal length f and brought to a focus, giving this system $f/\# = f/D$. This is depicted in Fig. 1, which shows the $x - z$ plane of a simple optical system that has cylindrical symmetry about the z axis.

While none of the rays in the $x - z$ plane shown in the diagram will result in y polarization (this is also true for x -polarized rays in the $y - z$ plane), the rays in this plane do result in a z

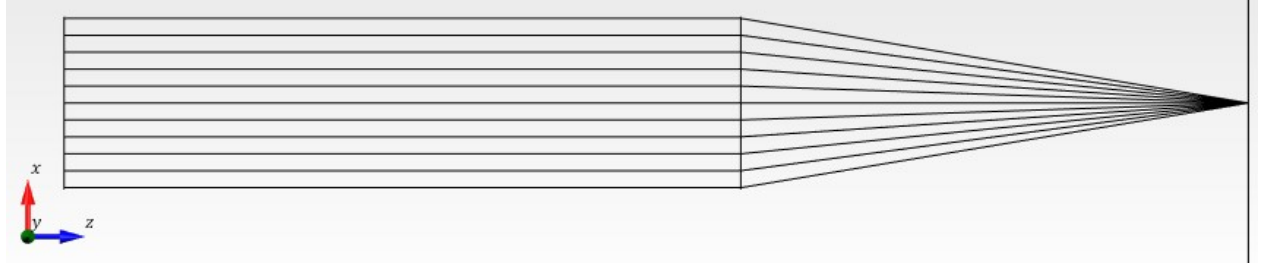


Fig 1 A simple $f/\# = 3$ optical system that brings rays to a focus with an idealized thin lens.

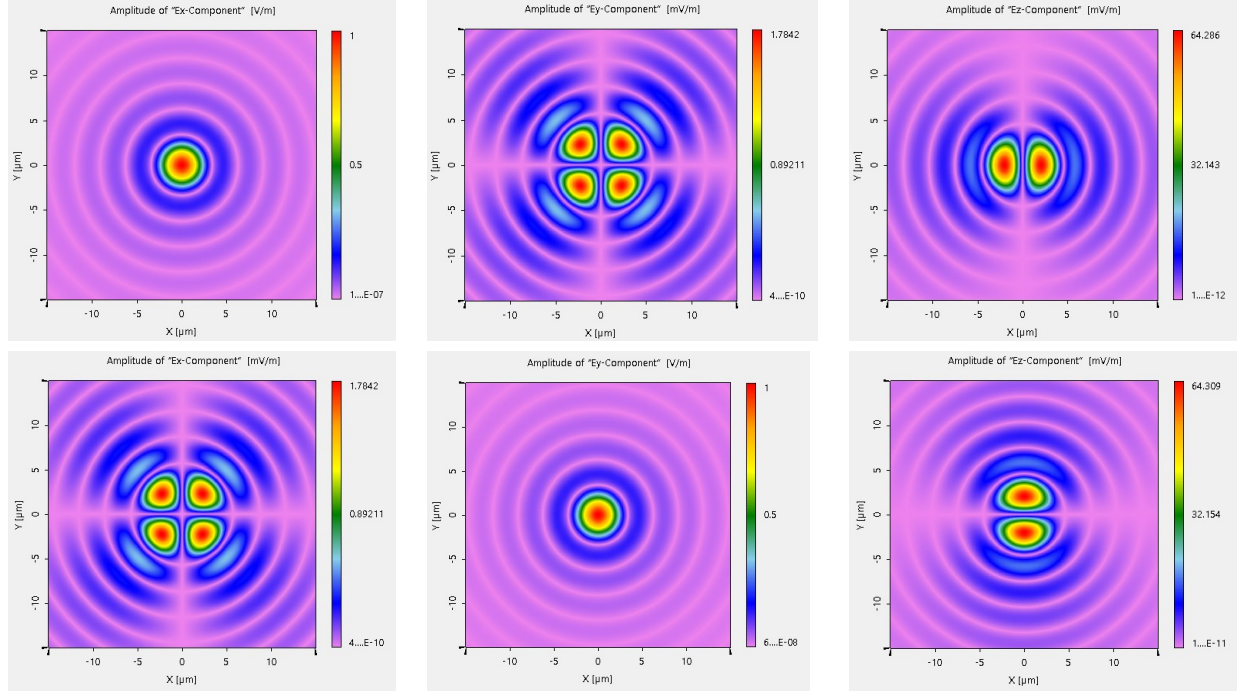


Fig 2 Focal plane electric fields corresponding to the $f/\# = 3$ optical system depicted in Fig. 1 [diameter $D = 10$ cm, focal length $f = 30$ cm, wavelength $\lambda = 1 \mu\text{m}$]. The top row shows $|E_x|$ (peak = 1 V/m), $|E_y|$ (peak = 1.8 mV/m), and $|E_z|$ (peak = 64 mV/m), respectively, when the input polarization is in the x direction. The bottom row shows $|E_x|$ (peak = 1.8 mV/m), $|E_y|$ (peak = 1 V/m), and $|E_z|$ (peak = 64 mV/m), respectively, when the input polarization is in the y direction. The dominant polarization is shown in the upper right and middle bottom; the others are cross-polarization. All field units are V/m and are normalized by a factor that makes the maximum of $|E_x|$ in the top row 1 V/m. The color scale in all images is linear. Note the symmetry in that $|E_x|$ in the top row is the same as $|E_y|$ in the bottom row and that $|E_x|$ in the bottom row is the same as $|E_y|$ in the top row.

cross-polarization component: Consider the ray in the diagram that hits the lens a distance x_0 from the z axis. The refraction angle of this ray, θ_0 is specified by $\tan \theta_0 = x_0/f$, and for a large $f/\#$ we approximate $\theta_0 \approx x_0/f$. To find the electric field vector of this ray just after it has been refracted by the lens, we must rotate the electric field vector of the collimated beam, $\sqrt{I}(1, 0, 0)$, about the y axis (because the ray is in the $x - z$ plane) by the angle θ_0 . The direction vector of the refracted electric field corresponding to this ray is $\hat{u} = (\cos \theta_0, 0, \sin \theta_0)$, and the electric field vector for this ray is simply $\hat{u}\sqrt{I}$.

The trigonometry is trickier when we treat rays that are not in $x - z$ or $y - z$ planes. If we

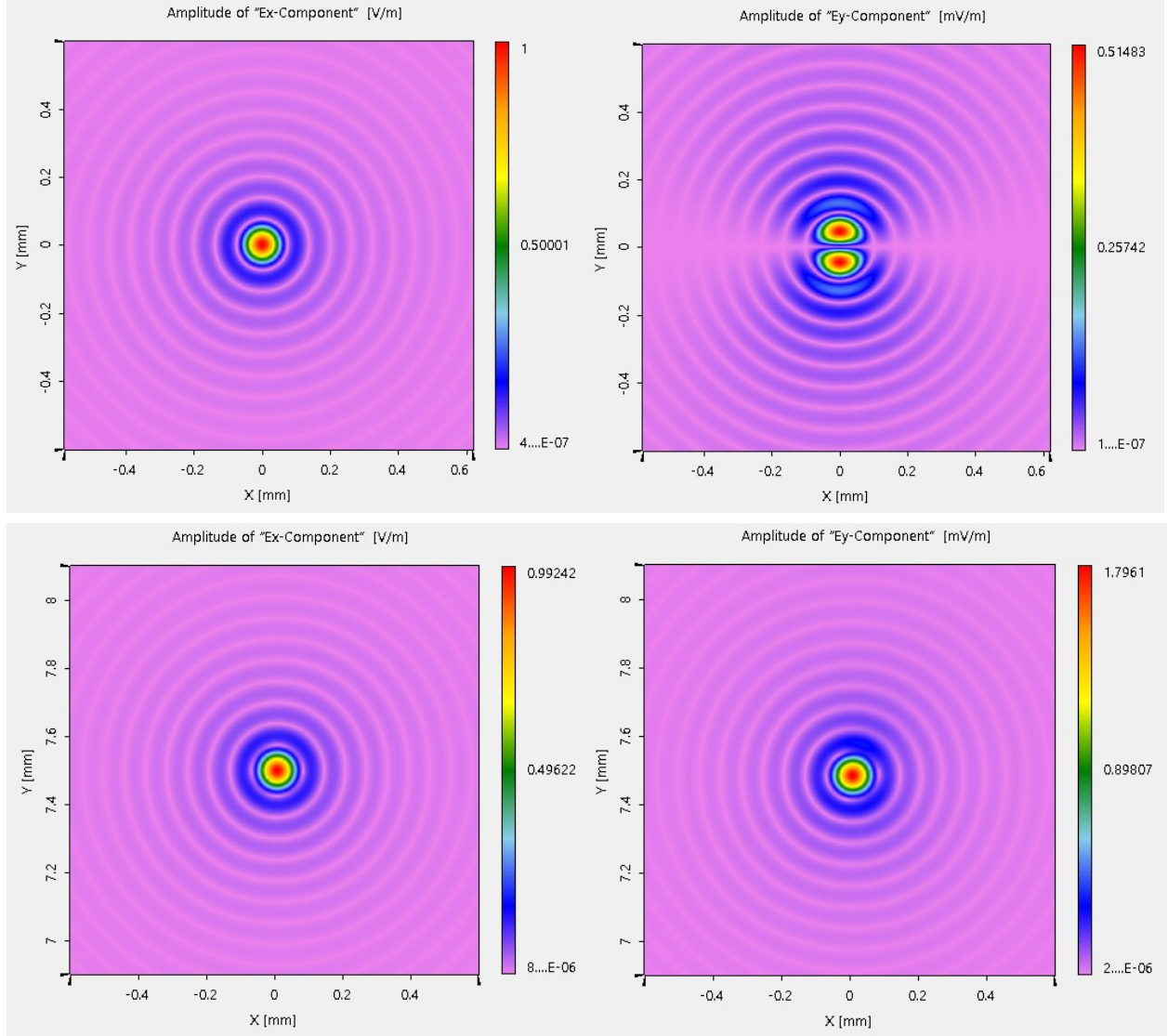


Fig 3 Focal plane electric fields corresponding to a collimated beam focused by a $f/ \# = 62.5$ OAP with an off-axis reflection angle of 20° . See text for details. The units of the linear color scale are V/m in the left column and mV/m in the right column. The values are normalized so that the peak of the upper left panel is 1 V/m. The upper row corresponds to an on-axis input beam (focal point at the origin), while the lower row shows results for an off-axis input beam with a focal point at $(0, 7.5 \text{ mm})$. The input beams in both cases are x -polarized. The two images on the left are dominant polarization and the two on the right are cross-polarization. The upper-left image shows $|E_x|$ (peak = 1 V/m) and the upper-right image shows $|E_y|$ (peak = 0.5 mV/m). The lower-left image shows $|E_x|$ (peak = 0.992 V/m), and the lower-right image shows $|E_y|$ (peak = 1.8 mV/m). Note the differences shown in the images on the right. There is no need to show results for y -polarized input beams, since the results are symmetrical as they are in Fig. 2.

consider an x -polarized ray in the collimated beam that hits the lens at a position $(x_0, y_0, 0)$ (taking $z = 0$ to be the plane of the lens), this ray is refracted by angle of θ_0 , where $\tan \theta_0 = \rho_0/f$ and $\rho_0 = \sqrt{x_0^2 + y_0^2}$. The direction of the refracted electric field is obtained by rotating the vector $(1, 0, 0)$ by the angle θ_0 about the axis defined by the direction vector $(-y_0, x_0, 0)/\rho_0$. Defining $\cos \psi_0 = x_0/\rho_0$ and $\sin \psi_0 = y_0/\rho_0$ the resulting unit vector in the direction of the electric field of the refracted ray is given by: [https://en.wikipedia.org/wiki/Rotation_matrix]

$$\begin{pmatrix} \cos \theta_0 + \sin^2 \psi_0 (1 - \cos \theta_0) \\ -\sin \psi_0 \cos \psi_0 (1 - \cos \theta_0), \\ -\cos \psi_0 \sin \theta_0 \end{pmatrix}. \quad (1)$$

On the other hand, if the collimated beam is instead y -polarized, the unit vector in the direction of the electric field of the refracted ray is given by:

$$\begin{pmatrix} -\sin \psi_0 \cos \psi_0 (1 - \cos \theta_0), \\ \cos \theta_0 + \cos^2 \psi_0 (1 - \cos \theta_0) \\ -\sin \psi_0 \sin \theta_0 \end{pmatrix}. \quad (2)$$

In Eq. (1), since the collimated beam is assumed to be x polarized, cross-polarization components are the y and z components. The x component is called the *dominant component*. Similarly, Eq. (2), the dominant component is the y component and the x and z components are the cross-polarization components. For the large $f/\#$ systems of interest, the most important term in the cross-polarization components shown in Eqs. (1) and (2) is $\sin \theta_0 \approx \rho_0/f \leq D/f$, which means the cross-polarization is essentially proportional to the $f/\#$.

1.1.1 Simulation Examples

The first example we present in this section corresponds to the optical system depicted in Fig. 1, which is a $f/\# = 3$ system with a numerically ideal lens. The second example is a realistic simulation of an off-axis parabola (OAP) with a much larger $f/\#$.

In the case of Fig. 1, “ideal” only means that the focusing is aberration-free (despite the extreme $f/\#$). Although such a small $f/\#$ would be useful in confocal microscopy, it is not useful for telescopes; however, it provides a helpful and relatively simple illustration of the cross-polarization phenomenon. Fig. 2 shows the corresponding magnitudes $|\text{fields}|$ in the focal plane, with the top row corresponding to x -polarization in the input beam, and y -polarization in the bottom row. It is important to notice that $|E_x|$ in the top row is the same as $|E_y|$ in the bottom row; these are the *dominant polarizations* defined in Sec. 1.2. Similarly, $|E_y|$ in the top row is the same as $|E_x|$ in the bottom row; these are the *cross-polarizations* also defined in Sec. 1.2. The analytical developments to follow will take advantage of this symmetry.

Fig. 3 shows simulations of $|E_x|$ and $|E_y|$ for a x -polarized collimated beam focused by an OAP. The diameter of the collimated input beam is 8 mm, the wavelength of the light is $1 \mu\text{m}$, and the OAP’s off-axis reflection angle is 20° with a focal length of 500 mm, giving the system $f/\# = 62.5$. The OAP material is silver with a thin glass coating. The simulation is designed so that an on-axis collimated input beam propagates in the $+z$ direction and the optical axis remains in the $x - z$ plane after the 20° reflection from the OAP. The upper pair of images in Fig. 3 corresponds to the on-axis input beam. Here, “on-axis” means that the initial propagation direction is purely in the $+z$ direction. The results for y -polarized input beams are not shown because they are perfectly

symmetrical, just as they are in Fig. 2. Unlike Fig. 2, the cross-field (E_y for x -polarized input) does not split into four quadrants, instead, it is split into 2 regions; this is due to the off-axis reflection breaking symmetry about the x -axis.

The lower pair of images corresponds to an off-axis input beam. For this beam, the initial propagation direction is $\hat{y} \sin \eta + \hat{z} \cos \eta$, where $\eta = -120 \lambda/D = -0.86^\circ$, which is why these images are centered at (0, 7.5 mm), rather than the origin of the detector plane. While the lower left image is similar to the upper left image (minor differences can be seen), the cross field shown in the lower right image is rather different than in the upper right image, including a peak value of $|E_y|$ more than three times greater. Additionally, while the upper right image exhibits a bimodal behavior, the lower right does not, nor does it exhibit the same symmetry about the x -axis. The small difference in the peak values in the images on the left is due to the angular dependence of the Fresnel reflection coefficients applied at the OAP surface. Again, the results for y -polarized input beams are not shown because they are nearly symmetrical.

1.2 Calculation of Intensities Including Cross-Polarization

This section provides mathematical derivation of intensity that includes cross-polarization. Consider an unpolarized beam of starlight at the entrance pupil of an imaging system. We will confine this discussion to quasi-monochromatic light at the wavelength λ . The unpolarized light can be divided into two orthogonal linear polarization components, A and B . The direction of A in the entrance pupil is chosen so that A -polarized light has its dominant polarization in the x direction in the detector plane where an image is formed. Similarly, the B direction is chosen so that B -polarized light has its dominant component in the y direction of the imaging plane. In other words, if we were to ignore the polarization effects of the imaging system, A -polarized light would result only in x -polarized light at the detector, and B -polarized light would result only in y -polarized light at the detector. In the examples given above, the y -axis does not change when the beam encounters the focusing optic, so the A direction is the x -axis and the B direction is along the y -axis. Of course, most astronomical imaging systems that have coordinate system transformations need to be taken into account in order to determine what the A and B directions happen to be.

The time-dependent electric field vectors in the entrance pupil corresponding to the A -polarized and B -polarized light are given by the functions $\hat{a} a(t) \exp(j2\pi\nu t)$ and $\hat{b} b(t) \exp(j2\pi\nu t)$, where $\nu = c/\lambda$ (c being the speed of light), \hat{a} and \hat{b} are orthogonal unit vectors in the A and B directions. $a(t)$ and $b(t)$ are complex-valued stochastic processes, called *envelope functions* that rapidly modulate the harmonic fields.¹² The envelope functions $a(t)$ and $b(t)$ satisfy the following conditions:

$$\mathcal{P}[a(t), b(t')] = \mathcal{P}[a(t)]\mathcal{P}[b(t')] \quad (3)$$

$$\overline{a(t)} = \overline{b(t)} = 0. \quad (4)$$

$$\overline{a(t)a^*(t)} = \overline{b(t)b^*(t)} = 1 \quad (5)$$

$$\overline{a(t)b(t)} = \overline{a(t)b^*(t)} = \overline{a^*(t)b(t)} = 0, \quad (6)$$

where the \mathcal{P} represents probability, the superscript $*$ indicates complex conjugation and the overbar indicates a time-average operator, which for the purposes of this article is equivalent to taking the mean of a stochastic process. In reality, integration over a finite amount of time is needed for Eqs. (4) through (6) to be effectively realized. We assume that the required integration times are much less than any currently possible detector frame rate (say, 10^{-4} s). Eq. (3) states that the

processes $a(t)$ and $b(t)$ are statistically independent. Eq. (4) states that envelope functions are zero-mean, and Eq. (6) states that the envelope functions are *incoherent*. In fact, Eq. (6) follows from Eqs. (3) and Eq. (4). Eq. (5) states that the envelope functions have a variance of unity.

It is clear that while A -polarized light mostly results in x -polarized light at the detector, there may also be some y and z polarized light as well. An analogous statement applies to B -polarized light. Assuming that the z direction is normal to the detector, we need not worry about the z polarization, so we will confine our attention to the x and y polarizations in the detector plane. Let E_x^A represent the x (dominant) component of the field that results from propagating the A polarization through the system, and let E_y^A represent the corresponding y (cross) component. Similarly, E_x^B and E_y^B , respectively, represent the cross and dominant fields that result from propagating the B polarization through the system. With these definitions, the time-dependent vector electric field at the detector is given by:

$$\mathbf{E}(t) = \hat{\mathbf{x}}[E_x^A a(t) + E_x^B b(t)] + \hat{\mathbf{y}}[E_y^B b(t) + E_y^A a(t)], \quad (7)$$

where the harmonic term $\exp(j2\pi\nu t)$ has been dropped.

The intensity in the detector plane corresponding to Eq. (7) is:

$$I = \overline{\mathbf{E}(t) \cdot \mathbf{E}^*(t)} \quad (8)$$

$$= I_x^A + I_x^B + I_y^B + I_y^A, \quad (9)$$

where \cdot represents a scalar (i.e., dot) product and $I_x^A = |E_x^A|^2$, $I_x^B = |E_x^B|^2$, $I_y^B = |E_y^B|^2$, $I_y^A = |E_y^A|^2$. The fact that the four terms in Eq. (7) result in four terms in Eq. (9) with no cross terms is due to the fact that $\hat{\mathbf{x}} \cdot \hat{\mathbf{y}} = 0$ and the incoherence conditions in Eq. (6).

2 Including Two Linear Polarizers

The major hurdle to estimating the weak cross intensity, which could potentially be confounded with incoherent intensity, is that only under the dark hole condition is the cross intensity not necessarily overwhelmed by the dominant intensity. Further, it is the authors' experience that it is not possible to significantly modulate the cross field for probing purposes (see below) without destroying the dark hole in the dominant intensity, which exists only under precise conditions. However, two linear polarizers, one in the collimated entrance beam, and another just before the detector can change this dynamic substantially. The concept is as follows:

- The linear polarizer in the entrance beam only allows A -polarized light to pass (see Sec. 1.2). This results in the dominant polarization being in the x -direction at the detector plane and the cross-polarization being in the y -direction [see Eq. (9)].
- The linear polarizer just before the detector only allows y -polarized light to pass, removing the dominant field; this allows the cross field to be measured.

The analysis provided below takes into account the fact that real polarizers have finite leakage, allowing small fractions, ϵ_1 and ϵ_2 (e.g., 10^{-5}), of the attenuated intensity to pass. We model the Jones matrix of the linear polarizer placed in the entrance pupil, in the AB coordinate system as:

$$H_{AB} = \begin{pmatrix} 1 & 0 \\ 0 & \sqrt{\epsilon_1} \end{pmatrix}. \quad (10)$$

Similarly, we model the Jones matrix in the xy coordinate system of the linear polarizer just before the detector as:

$$H_{xy} = \begin{pmatrix} \sqrt{\epsilon_2} & 0 \\ 0 & 1 \end{pmatrix}. \quad (11)$$

More realistic Jones matrix values would be a bit less than unity (say, 0.95) for the transmission axis, but we ignore that to reduce clutter. Applying these Jones matrices, Eq. (9) becomes:

$$I = \epsilon_2 I_x^A + \epsilon_1 \epsilon_2 I_x^B + \epsilon_1 I_y^B + I_y^A. \quad (12)$$

Thus, only the I_y^A component of the cross intensity is not attenuated by the polarizers. Importantly, under dark hole conditions, the dominant intensities, I_x^A and I_y^B , are severely attenuated as well. As an example, one of the glass dichroic linear polarizers from Polarcor has an extinction coefficient $\delta < 10^{-5}$ and operates from about $\lambda = 960$ to 1160 nm with less than $\lambda/4$ distortion. Of course, polarizers can be used in series to multiply their extinction factors, and this may be an attractive option. The distortion from the polarizers is not included in this analysis, but in the Discussion section, we argue that they should be manageable without undue complication.

3 Scalar Fourier Optics Approximations and Symmetry Considerations

Under the assumption that the light is unpolarized, the relationship between the scalar electric field u and the components of the vector field (E_x , E_y , E_z) is simply

$$E_z = 0, \text{ and } E_x = E_y = u/\sqrt{2}, \quad (13)$$

which is normalized so that the intensity value is consistent. Underlying standard Fourier optics principles, such as the Fourier transforming property of lenses, is the paraxial assumption that relies on the proximity of rays to the principal axis of the optical system.¹³ When the paraxial assumption does not hold, one must be prepared to reconsider Eqs. (13). Thus, if one is working in a regime accurately represented by Fourier optics, then, $E_x^A = E_y^B$ for the dominant fields, and $E_x^B = E_y^A = 0$ for the cross fields. Since all model-based EFC formulations successfully use Fourier optics,⁵ it follows that E_x^A and E_y^B are essentially the same and that the dark hole corresponds to small values of both $|E_x^A|$ and $|E_y^B|$. *En revanche*, the cross fields E_x^B and E_y^A arise due to non-paraxial effects, and simulations show that they are not substantially reduced in the process of creating the dark hole in the dominant field.

All of the calculations presented in this article are carried out without paraxial assumptions. The simulation results in Figs. 2 and 3 described above in Sec. 1.1.1 as well as those from the OAP-based coronagraph simulated in detail (described later) exhibited two symmetries for the dominant and cross fields. Interestingly, even beams off-axis by angles $100\lambda/D$ also showed these same symmetries. The following equations express the two symmetries:

$$|E_x^A| = |E_y^B|, \text{ and } |E_x^B| = |E_y^A|, \quad (14)$$

the former of which is consistent with scalar field assumptions. Of course, Eqs. (14) imply that $I_x^A = I_y^B$ and $I_x^B = I_y^A$.

Due to the above symmetry reasons leading to Eqs.(14), the models in this article need only treat light linearly polarized in the A direction entering the coronagraph. Thus, we will not calculate

E_x^B or E_y^B and will drop the A and B superscripts. We will take E_x and E_y to be the dominant and cross fields, respectively, in the detector plane. With this simplification, Eq. (12) becomes:

$$I = (\epsilon_2 + \epsilon_1)I_x + (\epsilon_1\epsilon_2 + 1)I_y \approx (\epsilon_2 + \epsilon_1)I_x + I_y. \quad (15)$$

Below, we will leverage the extinction factor $(\epsilon_2 + \epsilon_1)$ to allow us to apply DM commands that probe the cross field to the detriment of the dark hole in the dominant intensity.

4 A Matrix-Based Coronagraph Model

Let us represent the (A -polarized) field in the coronagraph DM plane, which is assumed to be located in the collimated beam from the entrance pupil, \mathcal{A} , as $U(\rho; \mathbf{c})$ where ρ is the 2D spatial coordinate vector in the pupil plane and \mathbf{c} is a vector of DM actuator commands, known as the *DM command* or, simply, *command*. Similarly, we represent the field in the detector plane as $\hat{x}E_x(\mathbf{r}; \mathbf{c}) + \hat{y}E_y(\mathbf{r}; \mathbf{c})$, where $E_x(\mathbf{r}; \mathbf{c})$ and $E_y(\mathbf{r}; \mathbf{c})$ are dominant and cross fields, respectively. Coronagraphs are linear optical systems in the sense that the beam does not pass through nonlinear gain media such as laser cavities. Due to linearity, we have the relationships for the dominant and cross fields:

$$E_x(\mathbf{r}; \mathbf{c}) = \int_{\mathcal{A}} d\rho \mathcal{K}_x(\mathbf{r}, \rho) U(\rho; \mathbf{c}), \quad \text{and} \quad (16)$$

$$E_y(\mathbf{r}; \mathbf{c}) = \int_{\mathcal{A}} d\rho \mathcal{K}_y(\mathbf{r}, \rho) U(\rho; \mathbf{c}), \quad (17)$$

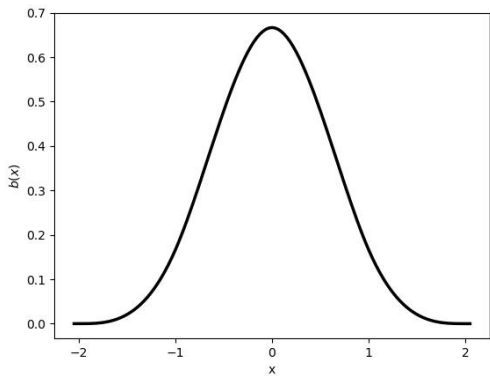


Fig 4 A cubic B-spline (CBS) basis function in 1D. Here, the width parameter $\delta = 1$. This function is supported on the interval $(-2\delta, 2\delta)$.¹⁶

Rodack and Frazin [14, 15] divided both the entrance pupil and the detector plane into pixels and modeled the system with a matrix equivalent of the kernel function $\mathcal{K}_x(\mathbf{r}, \rho)$. In the single DM coronagraph model presented here (described in more detail later), the field in the entrance pupil of the system is a plane wave modified by the DM. We simulate a DM with $\sqrt{N} \times \sqrt{N}$ actuators, each of which has an influence function modeled by a 2D cubic B-spline basis (CBS) function.¹⁶

As depicted in 1D in Fig. 4, the CBS looks much like a Gaussian. The CBS has a width parameter δ that is analogous to the standard deviation of a Gaussian. Unlike Gaussians, CBSs have finite extent in the spatial domain, yet they are well-behaved with usually negligible ringing under Fourier transformation. The 2D CBS is simply the tensor product of the 1D CBS with itself, i.e., $\eta(\rho) = b(x)b(y)$, where $\rho = (x, y)$ and $b(x)$ is the 1D CBS function. We model the field corresponding to the light reflecting off of the DM at the location ρ as:

$$u(\rho; \mathbf{c}) = \sum_{n=0}^{N-1} \eta(\rho - \rho_n) \exp(jc_n) \quad (18)$$

where ρ_n is the location of the center of the n th DM actuator, and the command vector \mathbf{c} , of length N , contains the phases c_0, \dots, c_{N-1} applied to the DM influence functions $\eta(\rho - \rho_0), \dots, \eta(\rho - \rho_{N-1})$. For convenience, although we call c_n the command for actuator n in this article, in reality, it is the phase corresponding to the command. Thus, assuming normal incidence on the DM, $c_n = 4\pi(h_n/\lambda)$, in which h_n is the commanded height for actuator n and λ is the wavelength. This somewhat nonstandard nomenclature will serve to reduce clutter.

In these simulations, the field in the entrance pupil was taken to be a 2D cubic B-spline basis function centered on a DM actuator, and the Virtual Lab Fusion (VLF) simulation package from LightTrans, Inc. performed non-paraxial propagation through the coronagraph to determine the resulting dominant and cross fields in all M detector pixels. Doing this for all N DM actuators results in the $M \times N$ complex-valued matrices $\tilde{\mathbf{D}}_x$ and $\tilde{\mathbf{D}}_y$. We denote the numerical model of the dominant and cross fields in the detector plane as $\mathbf{v}_x(\mathbf{c})$ and $\mathbf{v}_y(\mathbf{c})$, each of which has M components. Then, the model is captured by the matrix-vector equations:

$$\mathbf{v}_x(\mathbf{c}) = \tilde{\mathbf{D}}_x \mathbf{u}(\mathbf{c}) \quad \text{and} \quad (19)$$

$$\mathbf{v}_y(\mathbf{c}) = \tilde{\mathbf{D}}_y \mathbf{u}(\mathbf{c}), \quad (20)$$

where $\mathbf{u}(\mathbf{c})$ is a vector of N phasors with the n th component being $\exp(jc_n)$, so that $\mathbf{u}(\mathbf{c}_1 + \mathbf{c}_2) = \mathbf{u}(\mathbf{c}_1) \circ \mathbf{u}(\mathbf{c}_2)$, where \circ is the Hadamard (i.e. element-wise) product. Eqs. (19) and (20) are the model analogs of Eqs. (16) and (17). While VLF took a couple of days to create the matrices $\tilde{\mathbf{D}}_x$ and $\tilde{\mathbf{D}}_y$, the matrix-vector multiplications shown in Eqs. (19) and (20) are fast and ideally suited to iterative algorithms.^{17,18}

5 The Dark Hole

We start under the assumption that an EFC loop has already succeeded in creating a dark hole in a region on the detector region \mathcal{D} , which is a set of pixels, and let \mathbf{c}_0 represent the command corresponding to the dark hole configuration. In this article, we will only consider DM commands in the vicinity \mathbf{c}_0 , so it makes sense to economize the notation by redefining \mathbf{c} to be the difference between the DM command and \mathbf{c}_0 . Replacing \mathbf{c} with $\mathbf{c}_0 + \mathbf{c}$ in Eqs. (19) and (20) achieves this change of origin. Thus, we must replace $\mathbf{u}(\mathbf{c})$ with $\mathbf{u}(\mathbf{c}_0 + \mathbf{c}) = \mathbf{u}(\mathbf{c}_0) \circ \mathbf{u}(\mathbf{c})$. Note that the matrix-vector product $\tilde{\mathbf{D}}_x[\mathbf{u}(\mathbf{c}_0) \circ \mathbf{u}(\mathbf{c})] = [\tilde{\mathbf{D}}_x \text{diag}(\mathbf{u}(\mathbf{c}_0))] \mathbf{u}(\mathbf{c})$, where $\text{diag}(\mathbf{u}(\mathbf{c}_0))$ is a $N \times N$ diagonal matrix with the n th entry $\exp(jc_{0n})$. Next, we define $\mathbf{D}_x \equiv \tilde{\mathbf{D}}_x \text{diag}(\mathbf{u}(\mathbf{c}_0))$ so that Eqs. (19) and (20) become:

$$\mathbf{v}_x(\mathbf{c}) = \mathbf{D}_x \mathbf{u}(\mathbf{c}) \quad \text{and} \quad (21)$$

$$\mathbf{v}_y(\mathbf{c}) = \mathbf{D}_y \mathbf{u}(\mathbf{c}). \quad (22)$$

Eqs. (21) and (22) contain no approximations not already present in Eqs. (19) and (20). Just to be clear, $\mathbf{v}_x(\mathbf{0}) = \mathbf{D}_x \mathbf{1}$ and $\mathbf{v}_y(\mathbf{0}) = \mathbf{D}_y \mathbf{1}$, in which $\mathbf{0}$ and $\mathbf{1}$ are vectors of all zeros and ones, are the dominant and cross fields attained in the dark hole configuration.

Without confining ourselves to linearized analysis, we can replace $\mathbf{u}(\mathbf{c})$ with $\mathbf{1} + (\mathbf{u}(\mathbf{c}) - \mathbf{1})$ in Eqs. (21) and (22) and arrive at :

$$\mathbf{v}_x(\mathbf{c}) = \mathbf{v}_x(\mathbf{0}) + \mathbf{D}_x(\mathbf{u}(\mathbf{c}) - \mathbf{1}) \quad \text{and} \quad (23)$$

$$\mathbf{v}_y(\mathbf{c}) = \mathbf{v}_y(\mathbf{0}) + \mathbf{D}_y(\mathbf{u}(\mathbf{c}) - \mathbf{1}), \quad (24)$$

where $\mathbf{v}_x(\mathbf{0}) = \mathbf{D}_x \mathbf{1}$ and $\mathbf{v}_y(\mathbf{0}) = \mathbf{D}_y \mathbf{1}$ are the model fields at the dark hole configuration. Similarly, the true field can be expressed as:

$$\mathbf{f}_x(\mathbf{c}) = \mathbf{f}_x(\mathbf{0}) + \frac{\partial \mathbf{f}_x}{\partial \mathbf{u}}(\mathbf{u}_t(\mathbf{c}) - \mathbf{1}) \quad \text{and} \quad (25)$$

$$\mathbf{f}_y(\mathbf{c}) = \mathbf{f}_y(\mathbf{0}) + \frac{\partial \mathbf{f}_y}{\partial \mathbf{u}}(\mathbf{u}_t(\mathbf{c}) - \mathbf{1}), \quad (26)$$

in which $\mathbf{u}_t(\mathbf{c})$ is the unknown true field reflecting off of the DM, and the unknown Jacobians, $\partial \mathbf{f}_x / \partial \mathbf{u}$ and $\partial \mathbf{f}_y / \partial \mathbf{u}$, are constants due to the linearity of Eqs. (16) and (17). At this point in these developments, we have an exactly known numerical model, as summarized in Eqs. (23) and (24). In contrast, Eqs. (25) and (26) consist of unknown quantities, but their virtue is accurately representing the true optical system. We can hybridize Eqs. (23) and (24) and Eqs. (25) and (26) to arrive at what henceforth will be referred to as the *hybrid equations*:

$$\mathbf{f}_x(\mathbf{c}) \approx \mathbf{f}_x(\mathbf{0}) + \mathbf{D}_x(\mathbf{u}(\mathbf{c}) - \mathbf{1}) \quad \text{and} \quad (27)$$

$$\mathbf{f}_y(\mathbf{c}) \approx \mathbf{f}_y(\mathbf{0}) + \mathbf{D}_y(\mathbf{u}(\mathbf{c}) - \mathbf{1}), \quad (28)$$

which are nonlinear because $\mathbf{u}(\mathbf{c})$ is nonlinear. The validity of the hybrid equations relies on the hope that replacing $(\partial \mathbf{f}_x / \partial \mathbf{u})(\mathbf{u}_t(\mathbf{c}) - \mathbf{1})$ with $\mathbf{D}_x(\mathbf{u}(\mathbf{c}) - \mathbf{1})$ for the dominant field, and similarly for the cross field, are only misdemeanor offenses, at least when \mathbf{c} is sufficiently small. The fields, $\mathbf{D}_x(\mathbf{u}(\mathbf{c}) - \mathbf{1})$ and $\mathbf{D}_y(\mathbf{u}(\mathbf{c}) - \mathbf{1})$ and their linearized versions (see below), are known as *probe fields* or just *probes*.

Recalling that the n th element of $\mathbf{u}(\mathbf{c})$ is $\exp(jc_n)$, it follows that the linearization of $\mathbf{u}(\mathbf{c}) - \mathbf{1}$ is simply $j\mathbf{c}$. Working from Eqs. (27) and (28), the *linearized hybrid equations* are:

$$\mathbf{v}_x(\mathbf{c}) \approx \mathbf{v}_x(\mathbf{0}) + j\mathbf{D}_x\mathbf{c} \quad \text{and} \quad (29)$$

$$\mathbf{v}_y(\mathbf{c}) \approx \mathbf{v}_y(\mathbf{0}) + j\mathbf{D}_y\mathbf{c}. \quad (30)$$

Note that all EFC methods, except for the model-free one of Haffert et al. and the phase-retrieval-type approach of Malbet, Yu and Shao,^{19,20} rely on the validity of the linearized hybrid equation in the dominant field.^{5,21,22} It is likely that the accuracy of the linearized hybrid equation improves as the iterations approach the dark hole state.

6 Using Probes for Focal Plane Wavefront Estimation

The primary difficulty with probing the cross field is that the DM commands that probe the cross field effectively compromise the dark hole. Under the assumption of linearity, it is possible to

satisfy the dominant dark hole condition at a subset of pixels while probing the cross field, but, in practice, the linearity assumption is not satisfied for effective cross probes. Fig. 5, which shows I_x as a function of the amplitude of a probe command, depicts this concept. One of the probes chosen for the simulated estimations of the cross field (described later) was used to create Fig. 5. A probe amplitude of unity corresponds to the probe that was used for a measurement as part of the estimation process. The figure, which does not include the linear polarizers, shows that the dark hole is progressively destroyed as the probe amplitude increases. The linear polarizers can be taken into account by multiplying the y -axis by $(\epsilon_1 + \epsilon_2)$, as per Eq. (15).

Starting with the hybrid Eqs. (27) and (28), let the dominant and cross field probes be represented by the vectors $\mathbf{p}_x(\mathbf{c})$ and $\mathbf{p}_y(\mathbf{c})$, which can represent either the linearized (i.e., $j\mathbf{D}_x\mathbf{c}$ for the dominant field) or nonlinear variant [i.e., $\mathbf{D}_x(\mathbf{u}(\mathbf{c}) - 1)$ for the dominant field]. Using $\mathbf{p}_x(\mathbf{c})$ for the dominant probe field, multiplying the hybrid equation for the dominant field by its complex conjugate yields:

$$\begin{aligned} i_x(\mathbf{c}) = & \mathbf{h} + |\mathbf{f}_x(\mathbf{0})|^2 + |\mathbf{p}_x(\mathbf{c})|^2 \\ & - \Im(\mathbf{p}_x(\mathbf{c})) \circ \Re(\mathbf{f}_x(\mathbf{0})) + \Re(\mathbf{p}_x(\mathbf{c})) \circ \Im(\mathbf{f}_x(\mathbf{0})), \end{aligned} \quad (31)$$

where \Re and \Im indicate the real and imaginary parts, \mathbf{h} is the incoherent component, which is assumed independent of the DM command,* and \circ represents the Hadamard (i.e., element-wise) product. For the cross field, there is an equation similar to Eq. (31):

$$\begin{aligned} i_y(\mathbf{c}) = & |\mathbf{f}_y(\mathbf{0})|^2 + |\mathbf{p}_y(\mathbf{c})|^2 \\ & - \Im(\mathbf{p}_y(\mathbf{c})) \circ \Re(\mathbf{f}_y(\mathbf{0})) + \Re(\mathbf{p}_y(\mathbf{c})) \circ \Im(\mathbf{f}_y(\mathbf{0})), \end{aligned} \quad (32)$$

Note that Eq. (32) has no incoherent component, \mathbf{h} . This is because the incoherent source is assumed to be weak, making its cross-polarization signal negligible.

6.1 Regression Equations

Simply put, our aim is to use the hybrid equations [i.e., Eqs. (27) and (28)] to model probed intensities and estimate the real and imaginary parts of the unprobed cross field, $\mathbf{f}_y(\mathbf{0})$. Note that the use of the linear polarizers will extinguish the incoherent component \mathbf{h} in Eq. (31), the estimation of which could be done subsequently to obtaining an estimate of the cross polarization. The usual pairwise probing procedure in EFC methods uses DM commands that are small enough to allow estimation of the image plane field via linear regression. However, the DM commands we select to probe the cross field are too large to safely apply linear regression and we apply a nonlinear regression procedure described below. Nonlinear regression for the dark hole problem dates back to Malbet, Yu and Shao,²⁰ but they solved for a pupil-plane phase error, not the field in the focal plane, which makes their approach more closely related to classical phase retrieval.²³

Measuring the intensity with P different probe commands, $\mathbf{c}_1, \dots, \mathbf{c}_P$ enables the regression on the real and imaginary parts of the cross field in the dark hole, $\mathbf{f}_y(\mathbf{0})$. The corresponding dominant field $\mathbf{f}_x(\mathbf{0})$ could be estimated as well (with a sufficient number of probes), but the linear polarizers make this difficult, so it is better to estimate it without the polarizers in place. In the Discussion section, we outline a practical approach to adjust the dark hole command to account

*This is a good approximation so long as the DM modulations do not significantly alter the Strehl ratio.

for the wavefront error introduced by the polarizers. For simplicity, we consider only estimating the real and imaginary parts of the cross field, $\mathbf{f}_y(\mathbf{0})$. When we apply the linear polarizers as described in Sec. 2, the measured intensity in the detector pixels with probe command \mathbf{c}_i is:

$$\mathbf{y}_i = \epsilon \mathbf{i}_x(\mathbf{c}_i) + \mathbf{i}_y(\mathbf{c}_i) + \mathbf{n}_i, \quad 1 \leq i \leq P, \quad (33)$$

where $\epsilon = \epsilon_1 + \epsilon_2$, and \mathbf{n}_i is a vector of length M corresponding to noise that arises from the usual culprits, e.g., photon counting statistics, readout noise and thermal (dark) noise. Using Eqs. (31) and (32) in Eq. (33), we get

$$\begin{aligned} \mathbf{y}_i = \epsilon & [|\mathbf{f}_x(\mathbf{0})|^2 + |\mathbf{p}_x(\mathbf{c}_i)|^2 - \Im(\mathbf{p}_x(\mathbf{c}_i)) \circ \Re(\mathbf{f}_x(\mathbf{0})) + \Re(\mathbf{p}_x(\mathbf{c}_i)) \circ \Im(\mathbf{f}_x(\mathbf{0}))] \\ & + |\mathbf{f}_y(\mathbf{0})|^2 + |\mathbf{p}_y(\mathbf{c}_i)|^2 - \Im(\mathbf{p}_y(\mathbf{c}_i)) \circ \Re(\mathbf{f}_y(\mathbf{0})) + \Re(\mathbf{p}_y(\mathbf{c}_i)) \circ \Im(\mathbf{f}_y(\mathbf{0})) + \mathbf{n}_i, \end{aligned} \quad (34)$$

where we have dropped $\epsilon \mathbf{h}$ since this is a negligible quantity, and $1 \leq i \leq P$. Since we are taking $\mathbf{f}_x(\mathbf{0})$ to be known (or at least accurately estimated already), there are P measurement equations of the form shown in Eq. (34), from which we can estimate two unknowns (per pixel), $\Re(\mathbf{f}_y(\mathbf{0}))$ and $\Im(\mathbf{f}_y(\mathbf{0}))$. In these simulations, which use count rates one might expect from a 100 mW supercontinuum laser, each measurement had hundreds or thousands of counts per pixel, which mean we can neglect readout noise, and we can take the measured intensity \mathbf{y}_i as Poisson distributed to account for photon counting statistics. Because the measurements are statistically independent from one pixel to the next, the analysis to follow need only consider a single pixel in the dark hole, henceforth “the” pixel. Let k_i represent the number of counts measured with probe i in the pixel, so k_i is one of the components of \mathbf{y}_i . The two-component vector $\boldsymbol{\alpha} = (\alpha_1, \alpha_2)$ will represent the values obtained by $\Re(\mathbf{f}_y(\mathbf{0}))$ and $\Im(\mathbf{f}_y(\mathbf{0}))$ in the pixel, which are the quantities we will estimate. Let $s_i(\boldsymbol{\alpha})$ be the (unknown because $\boldsymbol{\alpha}$ is unknown) true intensity associated with probe i , for which we have the measured counts k_i . Thus, we have:

$$s_i(\boldsymbol{\alpha}) = \epsilon \mathbf{i}_x(\mathbf{c}_i) + \alpha_1^2 + \alpha_2^2 + |\mathbf{p}_y(\mathbf{c}_i)|^2 - \Im(\mathbf{p}_y(\mathbf{c}_i))\alpha_1 + \Re(\mathbf{p}_y(\mathbf{c}_i))\alpha_2, \quad (35)$$

where $\alpha_1^2 + \alpha_2^2 = |\mathbf{f}_y(\mathbf{0})|^2$, $\mathbf{i}_x(\mathbf{c}_i)$ is the value $\mathbf{i}_x(\mathbf{c}_i)$ obtains in the pixel [see Eq. (31)], and $\mathbf{p}_y(\mathbf{c}_i)$ is the value obtained by the cross probe field $\mathbf{p}_y(\mathbf{c})$ in the pixel. Assuming $s_i(\boldsymbol{\alpha})$ is in photon units, the probability of obtaining k_i counts under the Poisson distribution is $[s_i(\boldsymbol{\alpha})]^{k_i} \exp[-s_i(\boldsymbol{\alpha})]/k_i!$ The negative log-likelihood is:

$$\mathcal{Q}(\boldsymbol{\alpha}) = \sum_{i=0}^P [s_i(\boldsymbol{\alpha}) - k_i \ln(s_i(\boldsymbol{\alpha}))] \quad (36)$$

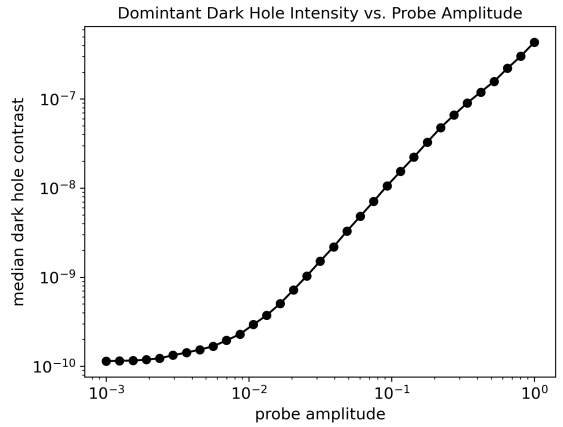


Fig 5 Dark Hole (dominant) intensity vs. probe amplitude for one of the probes used to estimate the cross field. A probe amplitude of unity corresponds to the amplitude used in the intensity measurement for estimating the cross field. This does not include the linear polarizers in the beam path. Including the polarizers amounts to multiplying the y -axis values by $(\epsilon_1 + \epsilon_2)$, as per Eq. (15). See Sec. 6 for details.

where $i = 0$ corresponds to an unprobed measurement (i.e., the dark hole state), and the $\ln(k_i!)$ term has been dropped since it does not depend on the estimated quantities, α . The estimate of α corresponds to a minimum of $\mathcal{Q}(\alpha)$, hopefully a global minimum. Using the symbol ∇ to represent the partial derivatives with respect to the components of α , it is useful to calculate $\nabla \mathcal{Q}(\alpha)$ for both employing gradient-based minimization algorithms and for calculating the Fisher information matrix (FIM) and its inverse: the Cramér-Rao bound.²⁴ Then,

$$\nabla \mathcal{Q}(\alpha) = \sum_{i=0}^P \left\{ \nabla s_i(\alpha) \left[1 - \frac{k_i}{s_i(\alpha)} \right] \right\}, \quad (37)$$

where $\nabla s_i(\alpha)$ can be found from Eq. (35). The Hessian, $\nabla \nabla \mathcal{Q}(\alpha)$, which is useful in Newton minimization methods, is easily obtained as well. The Cramér-Rao bound is a lower bound on the estimate error covariance for an unbiased estimator, and it proved to be an accurate estimator of the errors in the simulations shown below. A few lines of algebra show that under the Poisson distribution, the Fisher information matrix (FIM), denoted by F , takes an extraordinarily simple form:

$$F = \sum_{i=0}^P \frac{1}{s_i(\alpha)} \nabla s_i(\alpha)^T \nabla s_i(\alpha), \quad (38)$$

where T denotes the transpose operator and $\nabla s_i(\alpha)$ is taken to be a column vector, thus, Eq. (38) implies the outer product of the gradient vectors.

6.2 Nonlinear Estimation

The estimate of α , denoted as $\hat{\alpha}$, is taken to be the least of the multiple local minima of $\mathcal{Q}(\alpha)$ found by applying local minimization algorithms at multiple starting points. The unprobed, i.e., $i = 0$, measurement is critical for choosing the set of starting points for the algorithms. Referring to Eq. (35), first, notice that $p_y(0) = 0$ [see the remarks just before Eq. (31)]. Next, recall that the unprobed measurement corresponds to the dark hole state of the dominant field, which may have an intensity of, say, 10^{-10} in contrast units, without taking the linear polarizers into account. Including linear polarizers with an extinction factor of, for example, $\epsilon = 10^{-5}$, then the first term in Eq. (35) is $\epsilon i_x(0)$ is, perhaps, 10^{-15} . Therefore, the unprobed intensity is almost entirely the cross intensity, so, $s_0 \approx \alpha_1^2 + \alpha_2^2$, which may have a value somewhere around $10^{-13} - 10^{-11}$. The corresponding measured number of counts is y_0 , so we have $y_0 \approx \alpha_1^2 + \alpha_2^2$. In the simulations below, we performed N_{opt} local minimizations with the l th starting point being:

$$(\alpha_{1l}, \alpha_{2l}) = \zeta \sqrt{y_0} (\cos(\phi_l), \sin(\phi_l)), \theta_l = \frac{2\pi l}{N_{\text{opt}}}, 0 \leq l < N_{\text{opt}}, \quad (39)$$

where ζ accounts for the scaling between $\sqrt{\text{contrast}}$ units and $\sqrt{\text{photon count}}$ units of the field. In the simulations below, $N_{\text{opt}} = 24$ was used but a smaller number would likely have sufficed, and each of the N_{opt} starting points, we applied the conjugate gradient algorithm, with the analytical gradient from Eq. (37). The estimate error covariance matrix was taken to be the Cramér-Rao bound matrix, which is the inverse of the FIM shown in Eq. (38). The so-obtained error estimates are consistent with differences between the estimates and true values in these simulations. These nonlinear estimates and the error bar calculations are carried out rather quickly on a pixel-by-pixel basis and do not represent a significant computational cost.

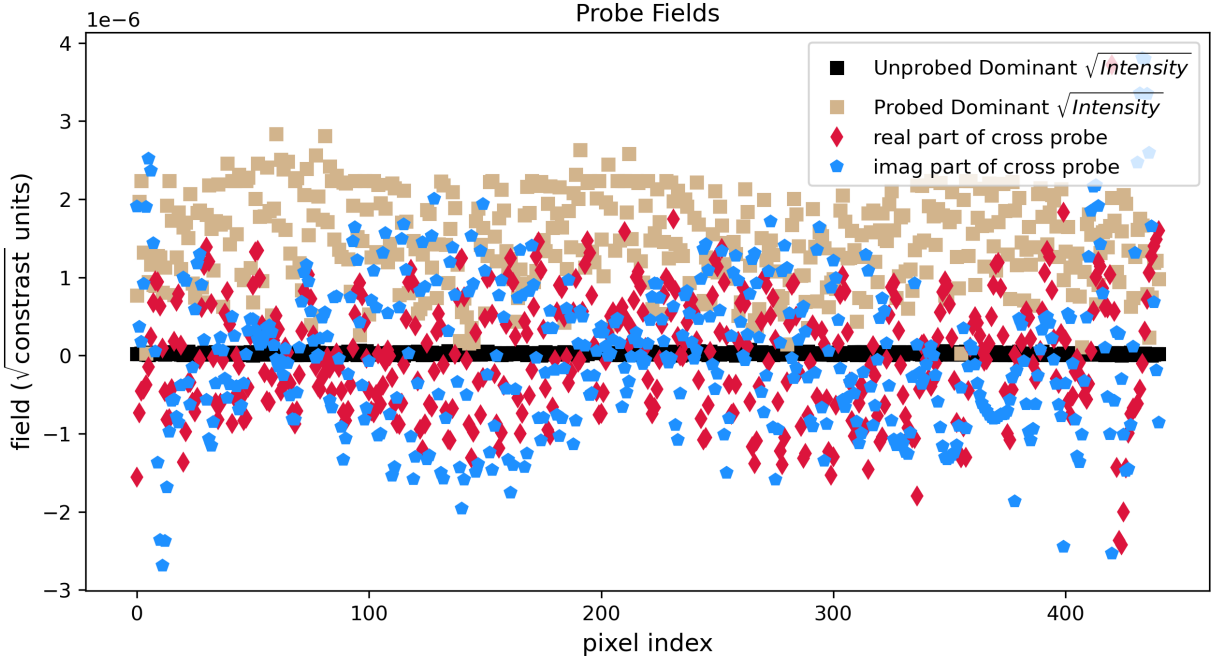


Fig 6 A simulation example of the dominant intensity and cross fields associated with one of the probes used for estimating the cross field in the dark hole. The x -axis is the pixel index within the dark hole (which has 441 pixels), and the y -axis is the electric field in units of $\sqrt{\text{contrast}}$. The red diamonds and blue pentagons correspond to the real and imaginary probe fields, respectively. The black and beige squares correspond to the square-root of the dominant intensity. The black squares are the values obtained with no probe applied (i.e., the dark hole state), and the beige squares are obtained when this probe is applied. The dominant $\sqrt{\text{intensity}}$ values include a linear polarizer extinction factor of $\sqrt{\epsilon_1 + \epsilon_2} = 2.24 \times 10^{-3}$.

6.3 Finding Informative Probes

The primary difficulty in probing the cross field is that the effective cross probe commands destroy the dark hole in the dominant field, as shown in Fig. 5 and Fig. 6, which leads to the cross intensity being swamped by the dominant intensity. This is unavoidable; hence, the use of the linear polarizers to remove most of the dominant intensity. The goal in this section is to find three probe commands that, when combined with the unprobed measurement, allow accurate estimation of the cross field in each pixel of the dark hole. The strategy employed in these simulations consists of several parts:

1. Find a set of $L > 3$ DM commands that correspond to local minima of a non-quadratic cost function that enforces desirable properties. (The simulations below used $L = 61$.) The cost function is given below in Sec. 6.3.1.
2. Given the L candidate solutions, evaluate the Cramér-Rao bound for all $\gamma = L!/(L-3)!3!$ possible solution triples. Note that the Cramér-Rao bound, \mathbf{C} , is a 2×2 matrix, evaluated for each dark hole pixel.
3. At each dark hole pixel, determine $\nu = \max[\text{diag}(\mathbf{C})]$, where the `diag` operator extracts the diagonal elements of a matrix, to get the worse of the error bounds on the estimates of the real and imaginary parts.

4. For each of the γ solution triples, find the “worst,” i.e., the largest, value of ν among all the dark hole pixels. Let us denote this value as ν_{\max} . ν_{\max} is the worst error bound of any of the estimated quantities in the dark hole.
5. Of the γ solution triples (see step 2 above), pick the “best of the worst”, i.e., the solution triple that has the smallest value of ν_{\max} . This is the solution triple chosen for the measurements.

Fig. 6 shows the result of one of the probe commands chosen using the simulations described in more detail later. The x -axis indexes the 441 pixels within the dark hole. The values in the figure include the effect of the polarizers on the dominant intensity. The dominant $\sqrt{\text{intensity}}$ in the dark hole state, i.e., the unprobed state, is depicted with black squares, which crowd the x -axis in the figure. The beige squares represent the dominant $\sqrt{\text{intensity}}$ when the probe is applied, and it can be seen that in most pixels this $\sqrt{\text{intensity}}$ is within a factor of several of the real and imaginary parts of the probe fields. Clearly, without the linear polarizers in place, which multiply the dominant $\sqrt{\text{intensity}}$ by about 0.0023, the cross probe fields would be completely overwhelmed by the dominant intensity. Of course, similar plots could have been provided for the other two probes chosen in this process. At a qualitative level, they do not look much different, but Cramér-Rao analysis in the above procedure ensures that the real and imaginary parts of the probe fields are sufficiently different to enable accurate estimates.

6.3.1 The Probe Cost Function

The L candidate solutions mentioned in step 1 are local minima of a cost function defined in this section. The cost function, $\mathcal{C}(\mathbf{c})$, includes several terms to encourage desirable properties in the probe command:

$$\mathcal{C}(\mathbf{c}) = -\mathcal{C}_{\text{ps}}(\mathbf{c}) + \mathcal{C}_{\text{dom}}(\mathbf{c}) + \mathcal{C}_{\text{amp}}(\mathbf{c}), \text{ , where} \quad (40)$$

$$\mathcal{C}_{\text{ps}}(\mathbf{c}) = \sum_{\text{pixels}} |\mathbf{p}_y(\mathbf{c})|^2 \quad (41)$$

$$\mathcal{C}_{\text{dom}}(\mathbf{c}) = \beta_{\text{dom}} \sum_{\text{pixels}} (i_x(\mathbf{c}) - t_{\text{dom}}) T(i_x(\mathbf{c}), t_{\text{dom}}) \quad (42)$$

$$\mathcal{C}_{\text{amp}}(\mathbf{c}) = \beta_{\text{amp}} \sum_{m=0}^{M-1} \{ (c_m - t_{\text{amp}}) T(c_m, t_{\text{amp}}) + (-c_m - t_{\text{amp}}) T(-c_m, t_{\text{amp}}) \} \quad (43)$$

where the sum over pixels refers to those in the dark hole, $T(\mu, \nu)$ is an indicator function that is zero when $\mu \leq \nu$ and unity otherwise, and c_m is the DM command corresponding to actuator m . The coefficients β_{dom} and β_{amp} , as well as the threshold values t_{dom} and t_{amp} , are tuning parameters chosen via a trial-and-error procedure. In Eq. (40), $\mathcal{C}_{\text{ps}}(\mathbf{c})$ rewards the strength of the cross probe intensity $|\mathbf{p}_y(\mathbf{c})|^2 = |\mathbf{D}_y(\mathbf{u}(\mathbf{c}) - \mathbf{1})|^2$ in its full nonlinear form. The function $\mathcal{C}_{\text{dom}}(\mathbf{c})$ penalizes the dominant intensity, $i_x(\mathbf{c})$, when it exceeds the threshold value t_{dom} ; it does not account for the effect of the linear polarizers. Note that $i_x(\mathbf{c})$ is not linearized here. The function $\mathcal{C}_{\text{amp}}(\mathbf{c})$ penalizes the DM actuator commands that exceed the threshold value t_{amp} , either positively or negatively. The value used here was $t_{\text{amp}} = \pi/4$. This serves as a form of regularization.

Eq. (40) is non-quadratic in its argument \mathbf{c} , and with $33^2 = 1089$ actuators in these simulations, it is not low-dimensional, so, it is not surprising that it has many local minima. However, for our

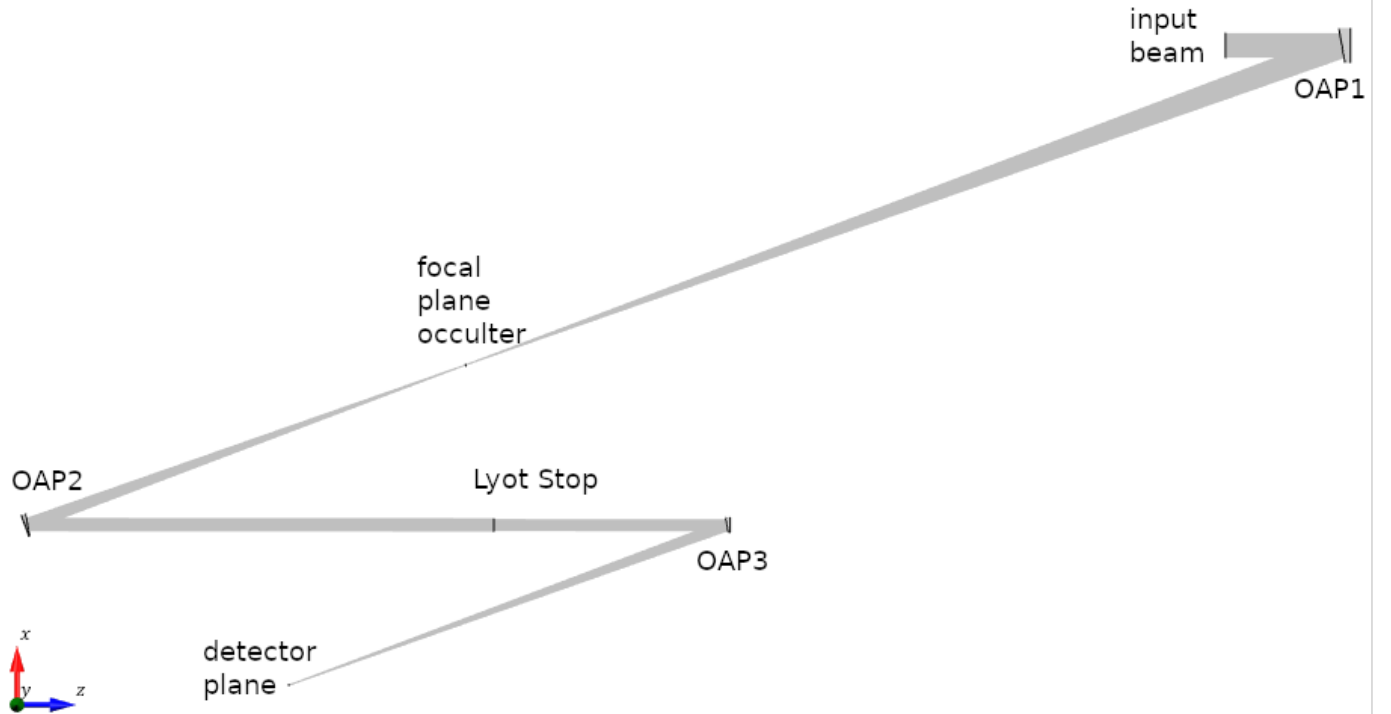


Fig 7 A schematic diagram of the Lyot-type stellar coronagraph used in these simulations. The DM, which is not shown, modulates the otherwise collimated input beam before OAP1.

purposes, having many local minima is a useful feature because each one is a possible probe choice, allowing us to select the most effective ones via the procedure outlined at the beginning of Sec. 6.3. The matrix-based representation of the optical system in Eqs. (21) and (22) enables rapid evaluation of $p_y(c)$ and $i_x(c)$ in Eqs. (41) and 42. This rapid evaluation capability is crucial because, even with the supplied analytical gradient, the conjugate gradient algorithm required approximately 500,000 function evaluations to converge to each local minimum. Each local minimum resulted from conjugate gradient steps starting with random values for the 1089 actuator commands.

7 Simulations and Results

All optical propagation computations were carried out using the VirtualLab Fusion (VLF) software from LightTrans, Inc. The simulation results in this article correspond to a square Lyot-type stellar coronagraph shown schematically in Fig. 7 and with key parameters summarized in Table 1. This coronagraph consists of 3 OAPs. The initial propagation direction of the beam before it encounters OAP1 is in the $+z$ direction. The simulation is configured so that the principal axis of the beam remains in the $x - z$ plane after each OAP encounter. With this arrangement, the y -axis is invariant throughout the system. Assuming no polarizers in the system, the consequence of this invariance is that y -polarized light in the input beam results in y -polarized light in the detector plane, weak polarization effects due to the finite $f/ \#$ notwithstanding. Similarly, if the light in the input beam is x -polarized it must also be x -polarized in the detector plane since it must be orthogonal to the global y - and local z -directions (again, weak polarization effects due to the finite $f/ \#$ notwithstanding). Thus, the A and B directions discussed in Sec. 1.2 correspond directly to the x and y axes in the input beam. To construct the \tilde{D}_x and \tilde{D}_y matrices introduced

in Sec. 4, VLF carried out 1089 propagations—one for each DM actuator-through the optical system. For each of these propagations, the input beam was x —polarized and set to one of the DM influence functions with an amplitude of unity. In the detector plane, the corresponding dominant field values, corresponding to a column of \tilde{D}_x , were the “ E_x ” values of the VLF output at each pixel, and the cross field values, corresponding to a column of \tilde{D}_y , were the “ E_y ” values.

Parameter	Value
wavelength (λ)	1 μm
input beam diameter (D)	19.34 mm
effective $f/\#$	44
DM actuators (spanning D)	33×33
occultor opaque diameter	240 μm
occultor transiton edge width	40 μm
Lyot stop clear diameter	9.1 mm
Lyot stop transition edge width	1.2 mm
OAP1 focal length (f)	800 mm
OAP2, OAP3 focal length (f)	400 mm
OAP1, OAP2, OAP3 off-axis angle (ζ)	20°

Table 1 Lyot coronagraph parameters used for the simulations.

then propagated to OAP1 ($f = 0.8$ m). Except for the DM modifications, the input beam is collimated. OAP1 focuses the beam on the focal plane occultor, which is an opaque square 240 μm ($5.8 f\lambda/D$) on a side, with a 40 μm wide border region over which the transmission smoothly goes from 0 to 1. OAP2 ($f = 0.4$ m) is placed 0.4 m from the first focal plane and it places the Fourier transform of the field in OAP1’s focal plane on the Lyot stop, which has a clear diameter of 9.1 mm and a transition border width of 1.2 mm. Then, OAP3 ($f = 0.4$ m) makes the coronagraphic image in the detector plane. The aberration-free, or *nominal*, PSF images corresponding to a plane wave input (which is simply a DM command of zero) for the dominant and cross intensities are provided in the top row of Fig. 8. Random phase and amplitude perturbations in the input beam created the aberrated images seen in the middle row of Fig. 8. The bottom row of Fig. 8 shows the aberrated PSFs with a dark hole in the dominant field with an area of $4 \times 4 (f\lambda/D)^2$. This dark hole contains 441 detector pixels. Given the known aberrated field in the detector plane from the simulation, determining a dark hole command was simply a matter of optimization. Fig. 9 provides a close up of the dark hole region in the dominant and cross intensities, where it can be seen that a dark hole in the dominant intensity does not correspond to a dark hole in the cross intensity.

To perform the estimation of the cross fields in the dark hole, we take a contrast of unity to correspond to 10^{15} photons/pixel/exposure. This is motivated by considering a common 100 mW continuous wave supercontinuum laser source that evenly distributes its power over a 1.6 μm wavelength range. A 3% bandpass filter, centered at the simulation wavelength of 1 μm , allows about 10^{16} photons/s to pass through. The linear polarizer extinction coefficients ϵ_1 and ϵ_2 were both taken to be 2.5×10^{-6} [see Eq.(15)], which is consistent with several off-the-shelf linear polarizers (also, sheet polarizers can be stacked). Fig. 10 shows the estimates of the real (left panel) and imaginary (right panel) parts of the cross field in each of the 441 dark hole pixels. The black squares are the true values and the red dots are the estimated values. The error bars

A square coronagraph was chosen for convenience of equally illuminating all of the 33×33 DM actuators. In Table 1, the “diameter,” D is the length of a side of the square, so, the initial beam area is D^2 . Since the purpose of this article is to introduce several new probing and analysis concepts on a mostly realistic simulated system, not to model a specific laboratory system in detail, such conveniences are justified.

As explained in Sec. 4, the DM is modeled using cubic B-spline influence functions and unit-amplitude phasor coefficients. The DM, which is not shown in Fig. 7 modifies the input beam, which is

extending through the red dots are the square-roots of the error covariance matrices estimated by the Cramér-Rao bound, as explained in Sec. 6.1.

8 Conclusions and Discussion

Cross-polarization effects are generally small, yet they are becoming more relevant as EFC progresses to ever greater contrast levels. This article proposes and simulates a set of laboratory procedures for EFC-style probing measurements of the cross-polarization effects in coronagraphic direct imaging systems. Developing the capabilities to measure the cross-polarization in a laboratory setting is likely to be critical for validating models of the cross-polarization. In these simulations, the probing and analysis procedures provided highly accurate estimates of the real and imaginary parts of the cross electric field within the dark hole, as shown in Fig. 10. Given the significant realism in these numerical simulations, these excellent results can be considered a demonstration of the viability of the proposed approach. Key elements of realism in the simulations include:

- The 3 OAP element Lyot coronagraph is designed with focal lengths and element sizes that are roughly similar to real testbed systems.
- The random phase/amplitude mask applied in the entrance pupil performs a role that is similar to defects on various optical surfaces.
- The simulation does not assume ideal linear polarizers in the sense that there is leakage of the orthogonal polarization into the beam.
- No linear approximations are used in the various calculations.
- The propagation of electric fields through the coronagraph is state-of-the-art and carried out with the VirtualLab fusion software.
- The probe intensity measurements are from a Poisson random number generator to account for photon counting noise, which is the only significant noise source due the large number of counts from the laser.

Of course, the ultimate goal of an exoplanet mission is to measure the planetary light, represented as the incoherent component \mathbf{h} in Eq. (31). On sky, regression equations similar to the ones presented in Sec. 6.1 could be modified in order leverage model predictions of the cross field in order to make more accurate estimates of the dominant field and incoherent intensity. Conveniently, the recent emphasis on digital twins provides opportunities for developing models of the cross field in the near future.¹⁰

A particularly useful form of model output would be a joint probability density function (PDF) of the real and imaginary parts of cross field, denoted as $\mathcal{P}(\text{cross field})$. Access to $\mathcal{P}(\text{cross field})$ would allow formulation of a likelihood function of the form: $\mathcal{P}(\text{measurements} | \text{incoherent intensity, dominant field, crossfield}) \times \mathcal{P}(\text{cross field})$, which could then be marginalized over the cross field to yield a likelihood function of the form: $\mathcal{P}(\text{measurements} | \text{incoherent intensity, dominant field})$. The latter could be maximized to yield an estimate of the incoherent intensity that fully accounts for the cross polarization. Although speculative, it is worth exploring the use of AI-based methods, such as convolutional neural networks, that predict the cross-polarization fields when the dominant field, likely measured with existing

EFC methods, is provided as an input. Mapping the dominant field to the cross field can be posed as an image translation problem, a problem well-suited to standard neural network (NN) architectures, such as the U-Net.²⁵ A digital twin of a coronagraph with random aberrations imposed could provide data sets for supervised learning to train such an NN. Note that there are a variety of methods that employ NNs to provide estimates of posterior PDFs.²⁶

The proposed experiment and analysis method for measuring the cross-polarization electric field in the dark hole combines has the following key elements:

- The use of linear polarizers to suppress the dominant polarization and enable measurement of the cross-polarization.
- The ability to self-consistently simulate the dominant and cross-polarization fields that arise due to various weakly polarizing effects in the optical system, including the finite $f/ \#$.
- Finding a set of candidate DM probes with the help of an optimization procedure. The optimization procedure given here accounts for leakage in the linear polarizers. This optimization procedure, in turn, is enabled by the next item:
- A method for rapidly calculating the image plane result of a DM command in both the dominant and cross fields, so that it can be carried out millions of times within a reasonable time frame (hours). In this article, the matrix-based optical system model fulfilled this requirement.
- A procedure for evaluating the most informative set of DM probes to be used in the measurements from the above set of candidate choices. Here, this was done with an exhaustive-search combined a Cramér-Rao analysis.
- A procedure for effective solution of the nonlinear regression equations to make the final estimates.

The required laboratory set-up is likely to be reasonably straightforward on current high contrast imaging test beds, requiring only fairly modest equipment such as linear polarizers and a 100 mW continuous-wave supercontinuum laser. In terms of carrying out a laboratory validation, a number of practical considerations come to mind:

- Laser fluctuations: The power output and the polarization state of lasers often fluctuate in time. Therefore, it is important to continually measure intensity of the beam after the first linear polarizer for the duration of the experiment. One option for this that might be considered is measuring the intensity of the light back-reflecting from the focal plane occulter or mask.
- Stray Light Contributions: The light not transmitted or absorbed by the linear polarizers needs to be rendered harmless. This may involve incarceration in light traps.
- The linear polarizers will introduce aberration to the wavefront, causing the dark hole command, c_0 to change when the polarizers are inserted. The dark hole command with both polarizers in place, c'_0 should obey the relationship: $c'_0 \approx c_0 + \varsigma_1 + \varsigma_2$, in which c_0 is the dark hole command without the polarizers, $c_0 + \varsigma_1$ is the dark hole command with only the

first polarizer in place, and $c_0 + \varsigma_2$ is the dark hole command with only the second polarizer in place. If necessary, the procedures provided in this article can be generalized to jointly estimate the dominant field in addition to the cross field.

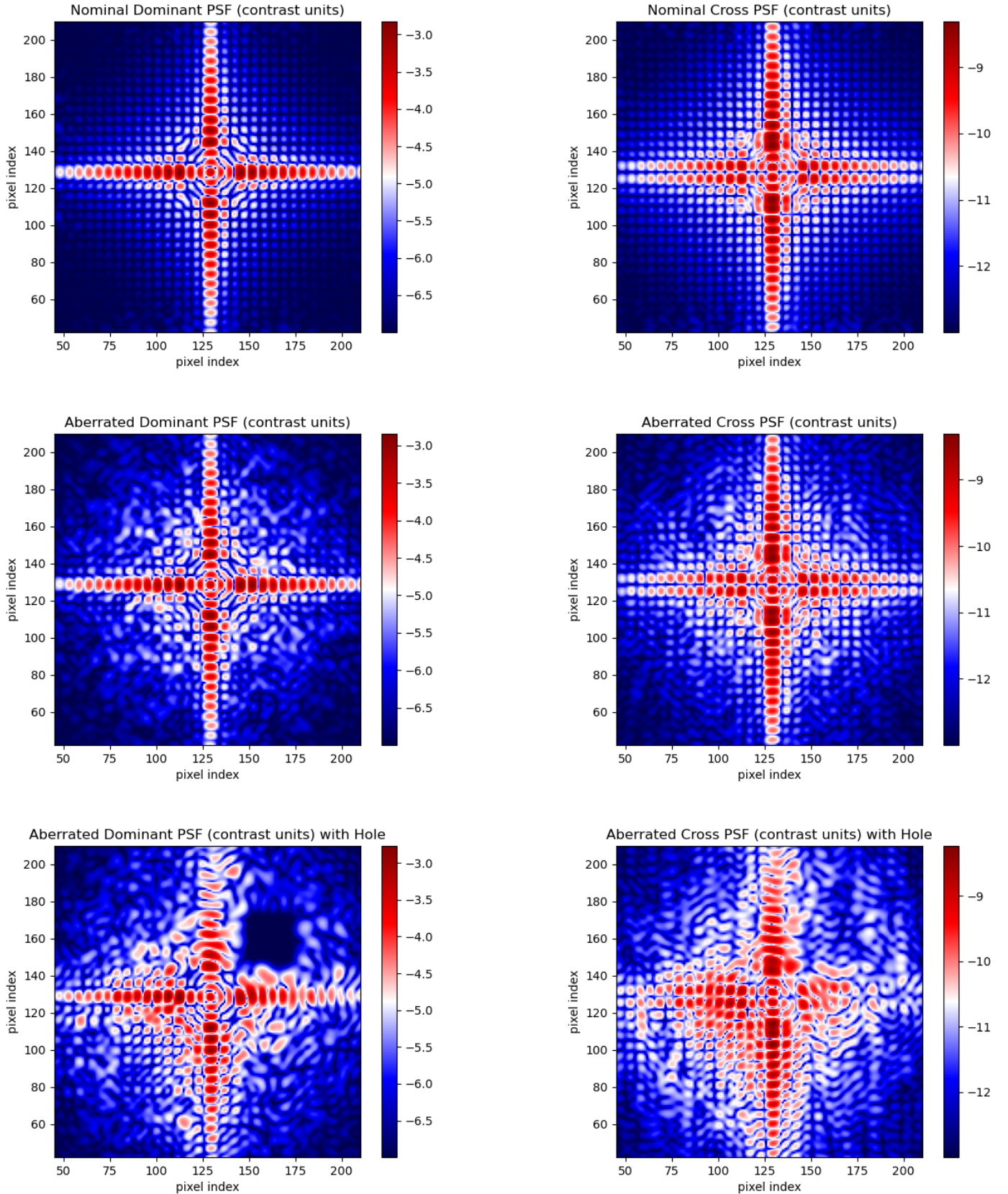


Fig 8 PSFs from coronagraph simulations. *Left column:* Dominant intensity (contrast units). These values do not include the effect of the linear polarizers. *Right column:* Cross intensity (contrast units). *Top Row:* Nominal (i.e., aberration free) model. *Middle Row:* Aberrated model. *Bottom Row:* Aberrated model with a dark hole of size $4 \times 4 (\lambda/D)^2$. In the bottom-left image, the color scale obtains its minimum value at 10^{-7} for display purposes. Note the dark hole in the dominant intensity does not correspond to a dark hole in the cross intensity.

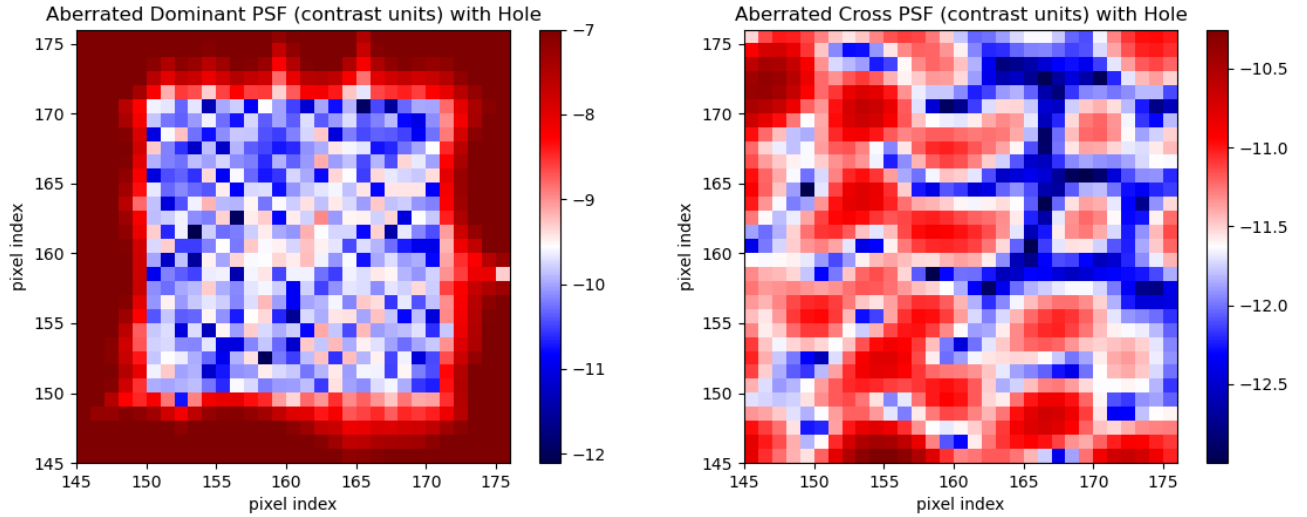


Fig 9 Close-ups of the $4 \times 4 (\lambda/D)^2$ dark hole region. *Left:* The dominant intensity (contrast units). *Right:* The Cross intensity (contrast units). These values do not include the effect of the linear polarizers. These are from the images shown in the bottom row of Fig. 8.

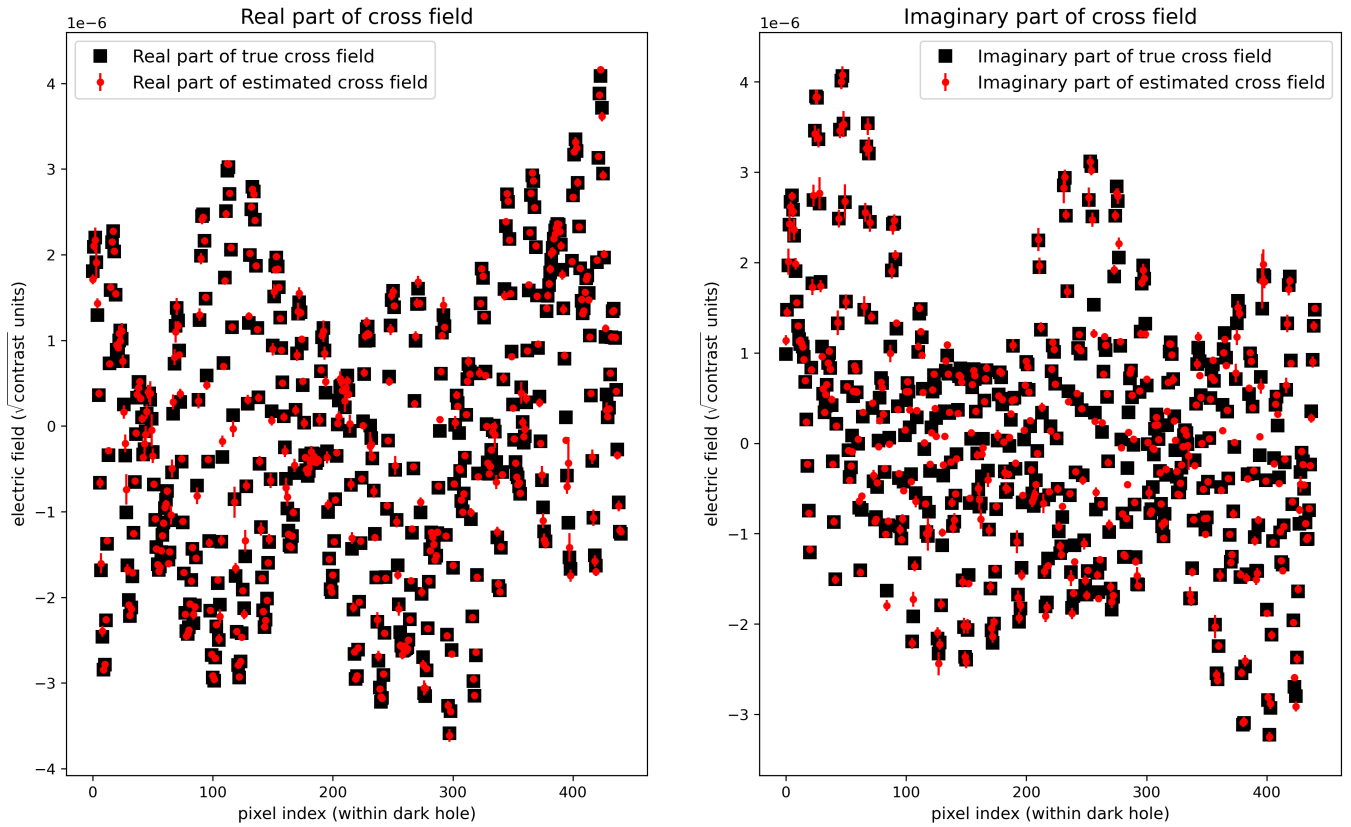


Fig 10 Estimated and truth values of the cross field in the dark hole region. *Left:* Real part of the cross field. *Right:* Imaginary part of the cross field. The black squares correspond to the true values of the fields and the red dots correspond to the probe-based nonlinear estimates described in the text. The error bars are square-roots of the variances estimated by the Cramér-Rao bound.

Acknowledgments

The author would like to acknowledge John Kohl, N. Jeremy Kasdin, Dan Sirbu and David Marx for helpful discussions. This work was funded by the Heising-Simons Foundation (grant numbers: 2020-1826, 2022-3912) and the National Science Foundation (award number: 2308352).

References

- 1 R. Juanola-Parramon, N. T. Zimmerman, L. Pueyo, *et al.*, “Modeling and performance analysis of the LUVOIR coronagraph instrument,” *Journal of Astronomical Telescopes, Instruments, and Systems* **8**, 034001 (2022).
- 2 C. Cavarroc, A. Boccaletti, P. Baudoz, *et al.*, “Fundamental limitations on Earth-like planet detection with extremely large telescopes,” *Astronomy and Astrophysics* **447**, 397–403 (2006).
- 3 J. E. Krist, J. B. Steeves, B. D. Dube, *et al.*, “End-to-end numerical modeling of the Roman Space Telescope coronagraph,” *Journal of Astronomical Telescopes, Instruments, and Systems* **9**, 045002 (2023).
- 4 A. Give’on, B. D. Kern, and S. Shaklan, “Pair-wise, deformable mirror, image plane-based diversity electric field estimation for high contrast coronagraphy,” in *Techniques and Instrumentation for Detection of Exoplanets V*, S. Shaklan, Ed., *Society of Photo-Optical Instrumentation Engineers (SPIE) Conference Series* **8151**, 815110 (2011).
- 5 T. D. Groff, A. J. Eldorado Riggs, B. Kern, *et al.*, “Methods and limitations of focal plane sensing, estimation, and control in high-contrast imaging,” *Journal of Astronomical Telescopes, Instruments, and Systems* **2**, 011009 (2016).
- 6 R. Belikov, D. Sirbu, D. Marx, *et al.*, “Laboratory demonstration of high contrast with the PIAACMC coronagraph on an obstructed and segmented aperture,” in *Space Telescopes and Instrumentation 2022: Optical, Infrared, and Millimeter Wave*, L. E. Coyle, S. Matsuura, and M. D. Perrin, Eds., *Society of Photo-Optical Instrumentation Engineers (SPIE) Conference Series* **12180**, 1218025 (2022).
- 7 B.-J. Seo, K. Patterson, K. Balasubramanian, *et al.*, “Testbed demonstration of high-contrast coronagraph imaging in search for Earth-like exoplanets,” in *Techniques and Instrumentation for Detection of Exoplanets IX*, S. B. Shaklan, Ed., *Journal of Astronomical Telescopes, Instruments, and Systems* **11117**, 599 – 609, International Society for Optics and Photonics, SPIE (2019).
- 8 M. Bottom, J. K. Wallace, R. D. Bartos, *et al.*, “Speckle suppression and companion detection using coherent differential imaging,” *MNRAS* **464**, 2937–2951 (2017).
- 9 P. Baudoz, C. Desgrange, R. Galicher, *et al.*, “Polarization effects on high contrast imaging: measurements on THD2 bench,” in *Space Telescopes and Instrumentation 2024: Optical, Infrared, and Millimeter Wave*, L. E. Coyle, S. Matsuura, and M. D. Perrin, Eds., **13092**, 130926L, International Society for Optics and Photonics, SPIE (2024).
- 10 S. Y. Haffert, V. Chambouleyron, V. Deo, *et al.*, “Congratulations, it’s twins: a digital twin for your high-contrast instrument? Part 2,” in *Adaptive Optics Systems IX*, K. J. Jackson, D. Schmidt, and E. Vernet, Eds., **13097**, 130976O, International Society for Optics and Photonics, SPIE (2024).

- 11 M. Born and E. Wolf, *Principles of Optics: Electromagnetic Theory of Propagation, Interference and Diffraction of Light*, seventh expanded edition, The Press Syndicate of the University of Cambridge (1999).
- 12 E. Collett, *Polarized Light: Fundamentals and Applications*, Marcel Drecker, Inc. (1993).
- 13 J. W. Goodman, *Introduction to Fourier Optics*, second edition, The McGraw-Hill Companies, Inc. (1996).
- 14 A. T. Rodack, R. A. Frazin, J. R. Males, *et al.*, “Millisecond exoplanet imaging: I method and simulation results,” *Journal of the Optical Society of America A* **38**, 1541 (2021).
- 15 R. A. Frazin and A. T. Rodack, “Millisecond exoplanet imaging: II regression equations and technical discussion,” *Journal of the Optical Society of America A* **38**, 1557 (2021).
- 16 M. Unser, “Splines: a perfect fit for signal and image processing,” *IEEE Signal Processing Magazine* **16**(6), 22–38 (1999).
- 17 S. A. Shakir, D. L. Fried, E. A. Pease, *et al.*, “Efficient matrix approach to optical wave propagation and Linear Canonical Transforms,” *Optics Express* **23**, 26853 (2015).
- 18 R. A. Frazin, “Efficient, nonlinear phase estimation with the nonmodulated pyramid wavefront sensor,” *Journal of the Optical Society of America A* **35**, 594 (2018).
- 19 S. Y. Haffert, J. R. Males, K. Ahn, *et al.*, “Implicit electric field conjugation: Data-driven focal plane control,” *A&A* **673**, A28 (2023).
- 20 F. Malbet, J. W. Yu, and M. Shao, “High-Dynamic-Range Imaging Using a Deformable Mirror for Space Coronography,” *Pub. Astron. Soc. Pacific* **107**, 386 (1995).
- 21 P. J. Bordé and W. A. Traub, “High-Contrast Imaging from Space: Speckle Nulling in a Low-Aberration Regime,” *Astrophysical Journal* **638**, 488–498 (2006).
- 22 A. Potier, A. J. Eldorado Riggs, G. Ruane, *et al.*, “Revisiting the Borde-Traub focal plane wavefront estimation technique for exoplanet direct imaging,” *arXiv e-prints* , arXiv:2408.14286 (2024).
- 23 E. J. Candès, X. Li, and M. Soltanolkotabi, “Phase retrieval: An overview of recent developments,” *IEEE Signal Processing Magazine* **32**(6), 98–109 (2015).
- 24 H. L. V. Trees, *Detection, Estimation, and Modulation Theory, Part I*, John Wiley & Sons, New York (1968).
- 25 O. Ronneberger, P. Fischer, and A. Becker, “U-net: Convolutional networks for biomedical image segmentation,” in *Medical Image Computing and Computer-Assisted Intervention*, 234–241, Springer (2015).
- 26 D. Barber, *Bayesian Reasoning and Machine Learning*, Cambridge University Press (2012).